Competing effects of temperature and mechanical stress on polar vortex transition in oxide superlattices

Pan Chen,[1,2,*,†] Xu Hou,[3,4,5,*] Jiandi Zhang,[1,6] Congbing Tan,[7,‡] Peng Gao,[2,§] Yan Liang,[1] Xuezeng Tian,[1] Lei Liao,[1] Xu-Sheng Yang,[3,5] Zhexin Jiang,[4] Zhi Xu,[1,8] Jie Wang,[4,9,‖] and Xuedong Bai[1,6,8,¶]

[1]*Beijing National Laboratory for Condensed Matter Physics, Institute of Physics, Chinese Academy of Sciences, Beijing 100190, China*

[2]*International Center for Quantum Materials, and Electron Microscopy Laboratory, School of Physics, Peking University, Beijing 100871, China*

[3]*Department of Industrial and Systems Engineering, Research Institute for Advanced Manufacturing, The Hong Kong Polytechnic University, Hung Hom, Kowloon, Hong Kong, China*

[4]*Department of Engineering Mechanics, Key Laboratory of Soft Machines and Smart Devices of Zhejiang Province, Zhejiang University, Zheda Road 38, Hangzhou, Zhejiang 310027, China*

[5]*The Hong Kong Polytechnic University Shenzhen Research Institute, Shenzhen 518060, China*

[6]*School of Physical Sciences, University of Chinese Academy of Sciences, Beijing 100049, China*

[7]*Hunan Provincial Key Laboratory of Intelligent Sensors and Advanced Sensor Materials, School of Physics and Electronics, Hunan University of Science and Technology, 411201 Hunan Xiangtan, China*

[8]*Songshan Lake Materials Laboratory, Dongguan, Guangdong 523808, China*

[9]*Zhejiang Laboratory, Hangzhou 311100, Zhejiang, China*

(Received 16 November 2023; revised 28 February 2024; accepted 21 October 2024; published 15 November 2024)

The interplay of different forms of energies in oxide superlattices, such as elastic, electrostatic, and gradient energies, can result in a stable long-range ordered polar vortex structure at room temperature. However, the role between these energies in determining the vortex structure still remains largely elusive due to the intricate interplay. By using a comprehensive *in situ* TEM apparatus and a prototype system, $PbTiO_3/SrTiO_3$ superlattice, we demonstrate that the vortex structure undergoes a first-order transition at the temperature around 653 K, while the application of in-plane mechanical stress at such a high temperature results in the reemergence of vortex structure. Cryogenic cooling to 94 K raises the stability of vortices, which would be destabilized by loading of out-of-plane mechanical stress. The results can be reproduced and well interpreted by phase-field simulations. These findings not only reveal the competing role of the temperature and mechanical stress at atomic scale but also demonstrate a feasible way to operate the vortex-based nanodevices working in harsh environments.

DOI: 10.1103/PhysRevB.110.195417

I. INTRODUCTION

The recent discovery of a long-range ordered vortices [1,2] in ferroelectric oxide superlattices has resulted in a fertile and rich playground for research to manipulate these states and explore their emergent properties [3–7] for different functionalities [8,9]. The stabilization of vortices is due to the interplay between Landau energy of the bulk, strain energy from the epitaxial substrate, gradient energy depending on the topology of polarization, and electrostatic energy from built-in fields [10,11]. These competing energies and multiple order parameters constitute a complex multidimensional free energy space [9]. Thus, how to understand the role between these parameters in determining the vortex transition path is a prerequisite for its practical applications.

According to the free energy formula, temperature, external mechanical stress, or electric fields can drive the vortices deviation from its equilibrium by perturbing the Landau energy, elastic, and electrostatic terms, respectively. Recent studies follow this formula and revealed that the vortices can be mechanically [12], electrically [13–15], or optically [16,17] manipulated to promote different switching dynamics. For examples, electric field driven vortex transition has been investigated theoretically [18,19] and experimentally [13,14,20] to accommodate the increasing electrostatic energy, while mechanical stress can align vortices to a-domain with increasing elastic energy [12]. Although the free energy of the vortex system is determined by multiple parameters, only a single term of them can now be manipulated to drive the vortex transition, hindering further explorations of the interactions between these parameters. For better understanding and control of vortices, it is necessary to unveil how the complex parameters/energies compete or cooperatively constitute the vortex energy space, which still remain largely exclusive.

*These authors contributed equally to this work.
†Contact author: panch@iphy.ac.cn
‡Contact author: cbtan@xtu.edu.cn
§Contact author: pgao@pku.edu.cn
‖Contact author: jw@zju.edu.cn
¶Contact author: xdbai@iphy.ac.cn

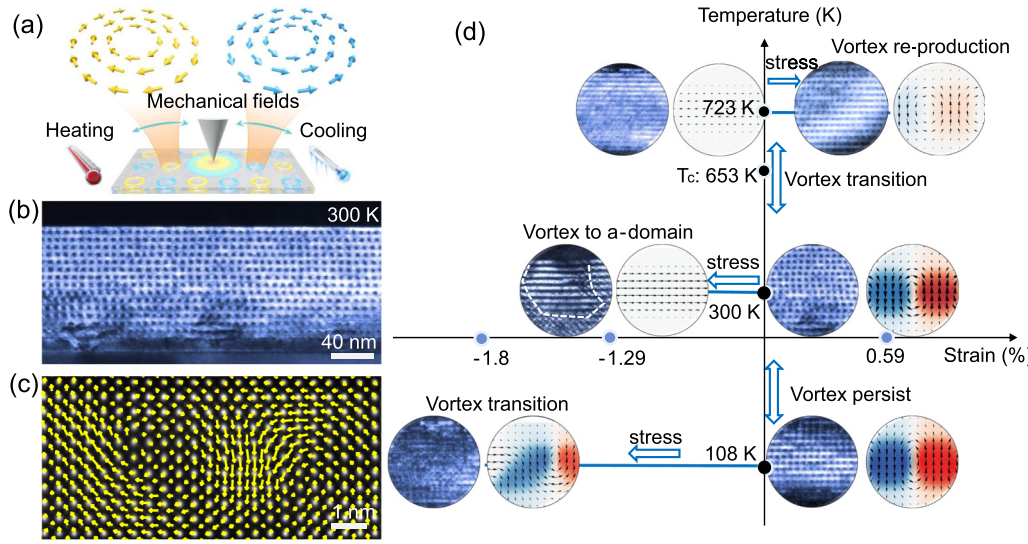

FIG. 1. Synergetic manipulation of vortices by temperature and mechanical stress. (a) A schematic of the synergetic multifield control of vortices. (b) A dark-field image of PTO/STO superlattices with the alternating dark and bright contrast showing the long-range order of vortices. (c) A clockwise and counterclockwise rotation vortex pair with the yellow vectors denoting the displacements between Pb/Sr and Ti. (d) A phase diagram of the vortex evolution with regard to strain and temperature. The circular image pairs represent the experimental dark-field images and simulated polarization configurations at different temperature and strain. The stress induced strain variation is labeled by SAED patterns.

Here, by using a comprehensive *in situ* platform in a transmission electron microscope (TEM) combined with phase-field simulations, we are able to explore the vortex evolution at the atomic scale under harsh environments, including low temperature and high temperature in conjunction with mechanical stress. We find that vortices disappear with the temperature increasing to 653 K, while application of a mechanical stress can restabilize it even at ∼723 K. In contrast, loading of mechanical stress at room temperature can only annihilate the vortices. Cryo-TEM demonstrates a stable vortex array at 94 K but can be destroyed by mechanical stress. Our work provides a fundamental phase diagram of vortices regarding to the temperature and strain which is the key to operating them at harsh or complicated environments. The demonstrated *in situ* multifield TEM also largely extends the capability to study the solid-state phase transition with multiple controllable parameters.

II. RESULTS AND DISCUSSION

The $PbTiO_3/SrTiO_3$ (PTO/STO) superlattices were grown on $(110)_0$ (the subscript *o* denotes orthorhombic notation) $DyScO_3$ (DSO) substrates with the $SrRuO_3$ as a buffer layer (see the Methods section in the Supplemental Material [21]). At room temperature (∼293 K), a long-range order of vortices can be demonstrated from the alternating bright and dark contrast in Fig. 1(b) and additional reflections in the selected area electron diffraction pattern (SAED) of Figs. S1(a) and S1(b) [21]. A clockwise and counterclockwise vortex pair in Fig. 1(c) exhibits the continuous rotating electric dipole demonstrated by the relative displacement between the Ti and Pb positions based on the atomically resolved high-angle annular dark-field (HAADF) scanning TEM (STEM) images. The corresponding out-of-plane lattice mapping in Fig. S1(c) [21] shows a sinusoidal wave, which in turn can be an indicator of vortex in the subsequent atomically resolved *in situ* experiment [12].

The PTO/STO films were then subjected to the cryogenic cooling, high temperature, and mechanical stimuli as schematically shown in Fig. 1(a). According to the evolution of vortices, a phase diagram in relation to stress and temperature is constructed in Fig. 1(d) to illustrate the interaction between temperature and strain.

For comparison, the vortice transition under mechanical stress at room temperature along out of plane were first reproduced and traced at atomic scale (Fig. S2 [21]), although demonstrated in our previous work [12]. In the low-temperature region, the cryo-dark-field image shows similar contrast to that at room temperature (Fig. S3 [21]), indicating the stability of vortices at low temperature. Such stability can also be demonstrated from the corresponding cryo-SAED pattern in Figs. S3(c)–S3(d) [21], which shows super-reflections from the vortex array. Loading of a mechanical stress to the superlattices along the film normal induces the transformation from vortices to regular ferroelectric domains, which is shown in time-series images in Fig. S3(e) [21]. With increasing the applied mechanical stress, the transition area extends through the films. Such a stress-driven phase transition at low temperature seems to bears resemblance to that at room temperature [12]. However, previous study demonstrated that in-plane polarization is favored to accommodate the increasing elastic energy, which is also manifested in dark-field images as the contrast directly becomes uniform, whereas here the residual contrast is exhibited in the dark-field images, indicating that the switching dynamics at low temperature tend to be different. At low temperature, the acquisition of reliable high-resolution HAADF images is hindered by the budding and vibrational drift arising from liquid nitrogen,

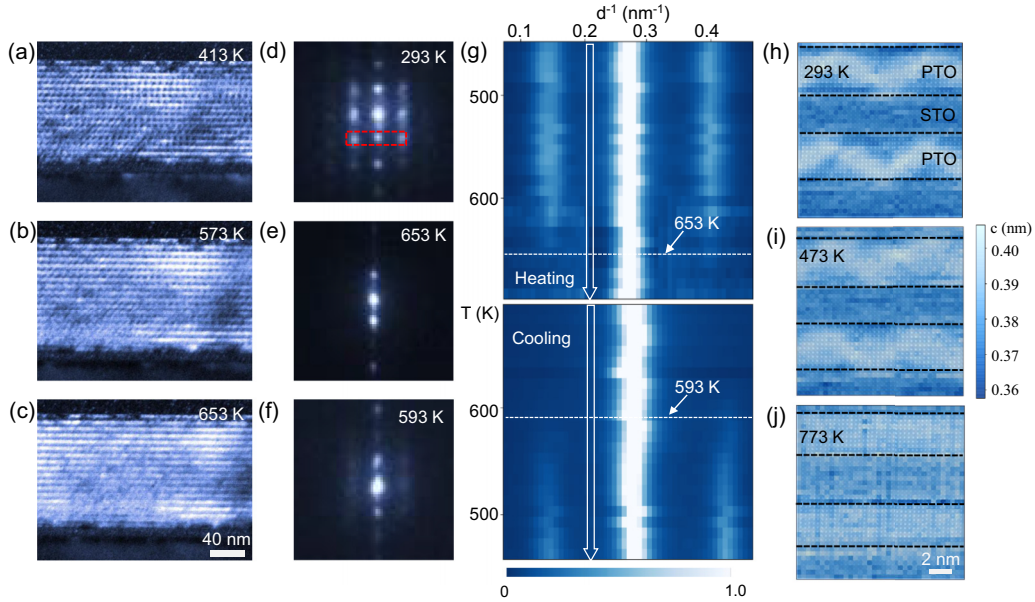

FIG. 2. The temperature-dependent vortex evolution. (a)–(c) A series of the dark-field images during the heating process, showing the absence of vortices at high temperature. (d)–(f) Enlarged $(001)_{pc}$ spots at heating and cooling process, indicating the evolution of vortices. (g) The vortex spots intensity as a function of temperature on heating and cooling process, showing the vortices start to disappear at 653 K and recovery at 593 K, respectively. The intensity is normalized by the central spot [red rectangle in (d) belongs to the lattice period]. (h)–(j) The out-of-plane lattice mapping overlaid on the HAADF-STEM images acquired at 293, 473, and 773 K, respectively.

making the direct polarization mapping and further elaborate analysis challenging in our experiments.

High temperature heating was then performed on the PTO/STO films via a microelectromechanical system chip holder (Fig. S4 [21]), which incorporates a scanning probe to apply external stimuli simultaneously. The great stability of this holder enables us to reach atomic resolution even at high temperature under mechanical loading. When the temperature increases in Figs. 2(a)–2(c), the vortex contrast gradually fades away, indicating a temperature-driven phase transition occurring at ∼653 K. On returning to room temperature, the vortices are recovered at ∼593 K (Fig. S5 [21]), which is 60 K lower than the transition temperature of the heating process. Thus, the response of the vortices to temperature is a reversible transition with a thermal hysteresis, indicative of a first-order phase transition, in agreement with the x-ray diffraction (XRD) results [13]. Note that our observations show that the transition or recovery occurred simultaneously at the whole film from the top surface to the bottom interface. Such a local tracking experiment cannot be done by the XRD.

The temperature-dependent SAED was obtained to probe the evolution of the vortices. The additional reflections of the $(001)_{pc}$ spots [Figs. 2(d)–2(f)] disappear and appear at 653 and 593 K, indicating the transformation and recovery of vortices upon heating and cooling, respectively. The reflection intensity of vortices as a function of temperature in Fig. 2(g) confirms the disappearance at ∼650 K and recovery at ∼590 K (Figs. S6 and S7 [21]), consistent with the result of the dark-field image. Previous investigations have found the transition from a mixed phase of vortices and a_1/a_2 to a pure a_1/a_2 phase through XRD when the temperature went up to ∼470 K [13], which is ∼180 K lower than the value of our observations. This discrepancy may arise from the different strain state between the samples because strain can lead to the enhanced Curie temperature [27,28]. The different sample thicknesses (PTO_{10}/STO_{10} in our sample and PTO_{16}/STO_{16} in Ref. [13]) and different sample geometry (the thin TEM lamellas with reduced dimension in our sample and bulk sample used for XRD detection [29]) result in distinguishable strain inside the films, which eventually determined the ferroelectric architectures and their transition temperature.

The thermal transition of vortices and the reversibility is further confirmed by the atomically resolved HAADF-STEM images. At room temperature, the vortex feature can be reflected by the out-of-plane lattice mapping, which exhibits a sinusoidal wave due to the continuous rotation of the lattice [Fig. 2(h)]. Such a sinusoidal wave can be sustained at 473 K as shown in Fig. 2(i). With the temperature increasing to 773 K [Fig. 2(j)], the wave contrast becomes uniform, indicating the vortex transition.

Based on the HAADF images, the atom positions can be determined [30,31] and thus the lattice can be extracted. We statistically measure the out-of-plane lattice c constant by fitting over 3000 unit cells for each temperature point (Fig. S8 [21]). In STO layers, the c lattice is enlarged with higher temperatures, resulting in a positive thermal expansion coefficient as shown in Fig. S8(h) [21]. The expansion coefficient $\alpha_{STO} = 1.02 \times 10^{-5}/K$, well consistent with the results revealed by XRD methods [32]. In contrast, the c lattice in PTO layer exhibits more intriguing thermal expansion behaviors. In the lower temperature range (300–573 K), the c lattice expands slightly with increasing temperature, showing a thermal expansion of $\alpha^{I}_{PTO} = 1.48 \times 10^{-5}/K$. As the temperature goes between 573 and 673 K, the c lattice of PTO demonstrates a contraction, leading to a negative

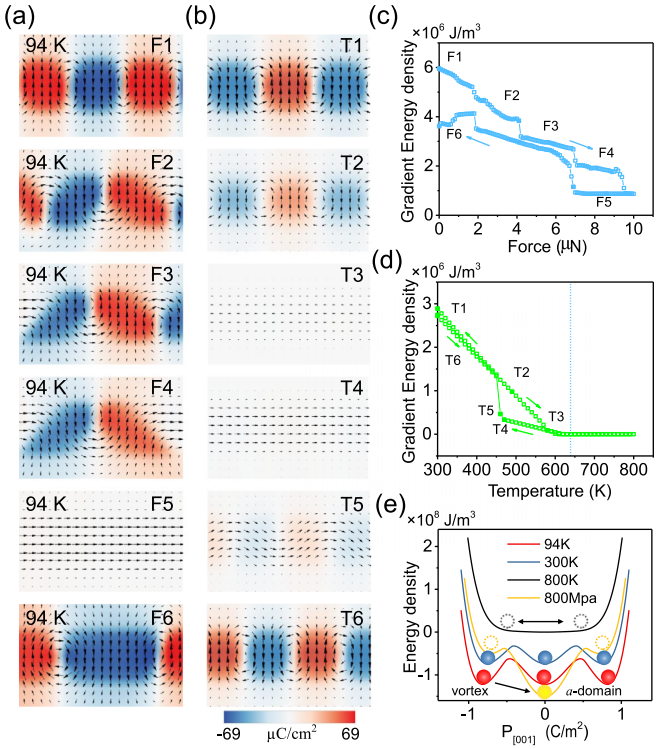

FIG. 3. Phase-field simulations revealed temperature and mechanical stress driven vortex transition. (a) Phase-field simulated vortex evolution under mechanical loading at 94 K. The notation F1–F6 labels different force states and the overlaying colors denote the magnitude of polarization. (b) The polarization switching dynamics under the heating and cooling process with the notation T1–T6 labels different temperatures and the overlaying colors denote the magnitude of polarization. (c) The gradient energy density is plotted as a function of mechanical loading at 94 K. (d) The gradient energy density is plotted as a function of temperature without external force. (e) Calculated energy profiles as a function of polarization when subjected to high temperature, low-temperature, and mechanical fields, showing the possible stable domain structure from the energy view under complicated conditions.

expansion coefficient $\alpha_{PTO}^{II} = -3.41 \times 10^5/K$. With the temperature continuously increasing to 723 K (Fig. S8 [21]), the lattice nearly keeps unchanged. It has been reported that the *c* axis linearly shrinks with temperature in a simple PTO film grown on DSO substrate [33], in sharp contrast with our observations. The subsequent anomalous lattice shrinkage behaviors arise from the vortex transition as it occurs exactly between 573 and 673 K. Once the transition is finished, the lattice would not change extensively.

Phase-field modeling captures the main features during the evolution of vortices at low temperature and unveils the underlying mechanism. As shown in Fig. 3(a), loading of mechanical stress leads to the shrinkage of out-of-plane components and expansion of in-plane components (F1–F3). Further increasing the mechanical stress could cause the formation of an *a*/*c*-domain-like structure (F4), and finally break the vortices into a uniform *a* domain (F5). With the unloading of mechanical stress, the vortices recover (F6).

Controllable and reversible transitions of polar vortex driven by high temperature can also be reproduced by phase field simulations, as shown in Fig. 3(b). Although the magnitude of polarization decreases, the increase of temperature is not able to break the vortices until the transition temperature is reached, resulting in a reduced uniform in-plane polarization (T1–T3). Upon cooling, the recovery of the vortices is accompanied by the rotation of the in-plane polarization and the formation of the dipole wave [34] (T4–T6).

The evolution of vortices can also be reflected from the gradual energy drops and recovery of the gradient energies, which is linked to the domain wall or polarization inhomogeneity. At low temperature, the application of mechanical stress gradually forces the continuously rotating electric dipole into uniform in-plane polarization, leading to a steplike decrease in gradient energies, while the unloading process exhibits a gradual increase before the reformation of vortices [Fig. 3(c)]. At high temperature, the gradient energy linearly decreases with the gradual transition of vortices and undergoes a sharp increase when the dipole wave suddenly transitioned into vortices in the cooling process [Fig. 3(d)].

The underlying mechanism of the domain evolution can be revealed from the analysis of energies. According to the Ginzburg-Landau formula, at low and room temperature, for example, 94 and 300 K [Fig. 3(e)], the energy landscape is identical for in-plane and out-of-plane components, thus stabilizing the vortex state. An increase of temperature to 800 K can modify the energy profile and drive the transformation of vortices. A loading of mechanical stress at 94 K can drive the energy profile from the balanced state, lowering the energy for in-plane polarization and raising the energies for out-of-plane polarization. Therefore, loading of mechanical stress will finally transform the vortices into the single *a* domain even at extremely low temperature.

Having established phase evolutions of vortices for temperature and stress at low temperature, we now simultaneously apply a mechanical stress at high temperature. The superlattices were subjected to in-plane mechanical stimuli as schematically shown in Fig. 4(a) by a scanning tungsten tip at 723 K, when the vortices already disappeared. A time series of dark-field images [Figs. 4(b)–4(d)] demonstrates the reformation of the alternating bright and dark contrast, indicating the recovery of vortices underneath the tungsten tip with mechanical loading. With the unloading of the stress, the vortex order gradually disappears and the film converts to a uniform contrast [Figs. 4(e)–4(g)]. This can be further confirmed by the SAED pattern acquired from the recovered region, i.e., the additional reflections from the vortex array are clearly distinguished [Figs. 4(h)–4(k)]. The atomically resolved HAADF image obtained before and under external stress with the geometric phase analysis shows the absence and presence of the sinusoidal wave (Fig. S9 [21]), respectively, suggesting the emergence of vortex order under loading at high temperature. The thermal effects caused by the contact of the tip to the sample is proved not enough to produce a vortex at high temperature (Fig. S10 [21]).

The distinct responses of polar vortex under mechanical stress at low temperature and high temperature indicate the competing role of strain and temperature. The lattice param-

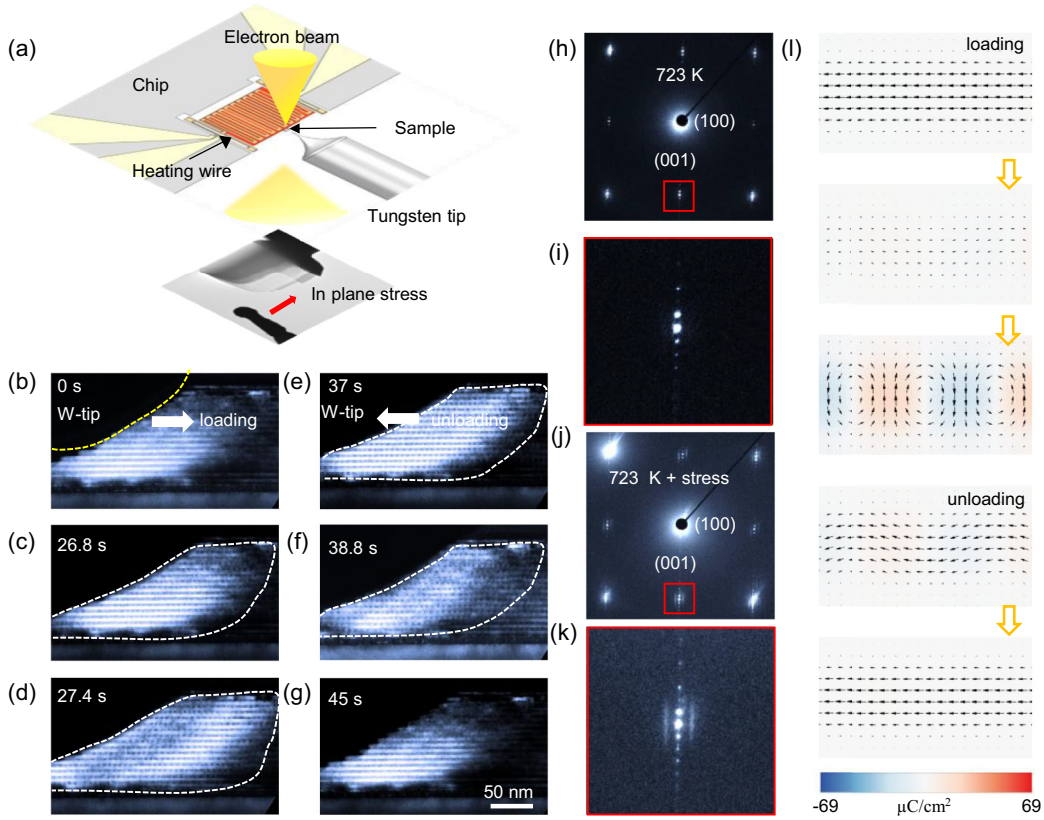

FIG. 4. Competing effect of mechanical stress and high temperature. (a) A schematic of the experimental setup incorporating heating chip and mechanical indenter. (b)–(g) A sequence of dark-field images with mechanical loading (b)–(d) and unloading (e)–(g) at 723 K, which is above the transition temperature for vortices. The dashed outlines highlight the region with clear vortex arrays. (h)–(k) The SAED pattern and enlarged $(001)_{pc}$ spots at high temperature (h), (i) without and (j), (k) with mechanical loading, respectively. The additional spots recovered under mechanical stress, indicating the re-emergence of vortices. (l) Phase-field simulation of the vortex production at high temperature.

eters as a function of temperature are demonstrated in Fig. 5. Upon heating, the out-of-plane c lattice shrinks and the in-plane lattice a expands, causing a strain variation of -0.38% and 0.39% along out of plane and in plane, respectively, which is in agreement with the results obtained by lattice statistics in Fig. S8 [21]. In contrast, cryogenic cooling leads to a larger c and smaller a with strain change of 0.23% and -0.2% along out of plane and in plane, respectively. Furthermore, the lattice parameters of the superlattice films can be calculated before and under mechanical loading, showing that the strain variation induced by the mechanical stress is 0.59%, -1.29%, and -1.8% at 723 K, room temperature and 108 K, respectively (Fig. 5 and Table I).

TABLE I. The lattice and strain variation with mechanical loading.

	c/Å	a/Å	Out-of- plane strain	In-plane strain
108 K	3.946	3.885	0.23%	−0.20%
108 K + stress	3.875	3.943	−1.8%	1.49%
300 K	3.937	3.893	0	0
300 K + stress	3.886	3.932	−1.29%	1.0%
723 K	3.922	3.908	−0.38%	0.39%
723 K + stress	3.945	3.920	0.59%	0.31%

There are several implications of our findings on the role of stress and temperature. First, the revealed competing role of temperature and strain shed insight on the underlying formation mechanism of the vortex, which now is phenomenologically considered as an interplay of complex energies (Landau, elastic, gradient, and electrostatic energies). Second, strain is an intermedia that bridges the competing of temperature and mechanical stress as application of in-plane stress could change the strain in a way contrary to the high temperature effect and drive the system back to the vortex state, while loading of a larger out-of-plane stress would reverse the strain caused by low temperature and destroy the vortices. Finally, such a competing role is related to the structure of PTO and screening of STO. The increasing temperature causes a reduced tetragonality and out-of-plane polarization [35] that can be fully depolarized by the STO layer, driving in-plane polarization at high temperature. Loading of in-plane stress enhances the tetragonality and out-of-plane polarization, which is not fully compensated by STO and results in a vortex with reduced magnitude of polarization.

III. CONCLUSION

In summary, we demonstrated that vortices can be manipulated by controlling at least one term of the energy contributions from Landau, elastic, and electrostatic energies in our

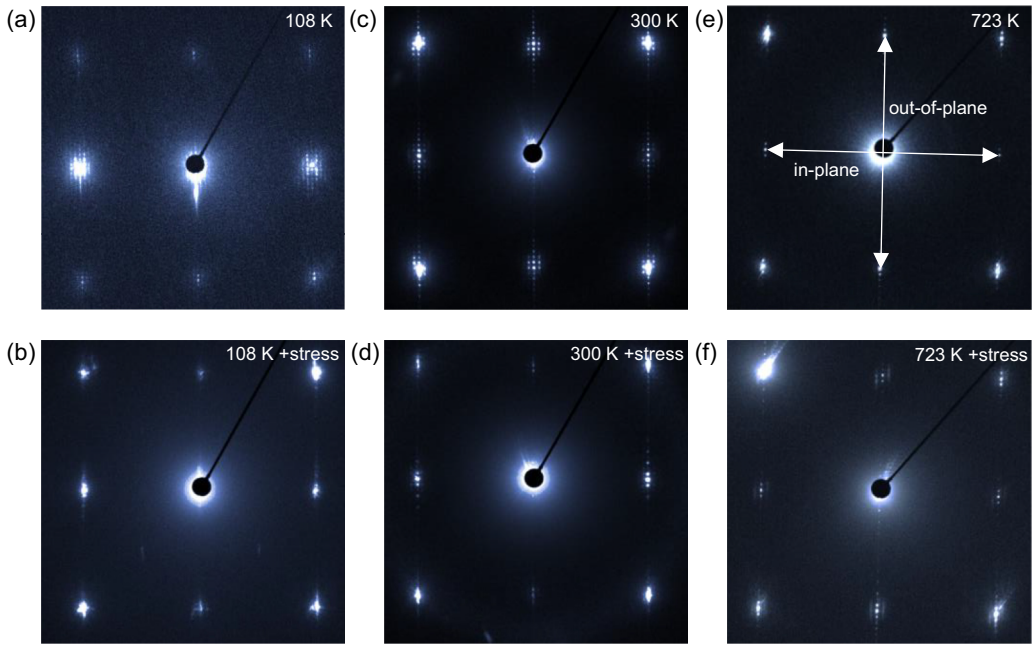

FIG. 5. Lattice and strain analysis during the cooling, heating, and mechanical loading. (a)–(f) The SAED patterns obtained before and under mechanical stress at 108 K (a), (b), 300 K (c), (d), and 723 K (e), (f), respectively. According to the SAED, the in-plane and out-of-plane lattice of the superlattices can be measured and thus calculate the strain change with temperature change or mechanical loading as shown in Table I. The calculated value by out-of-plane lattice is a little larger than that calculated by in-plane lattice due to the clamping effect of DSO substrate. Note the strain calculated by in-plane and out-of-plane lattice is opposite for 300 and 108 K but the same sign at 723 K, which may be the effects of negative Poisson coefficient. Therefore, the data obtained by out-of-plane lattice were taken to avoid any ambiguity. The calculated parameters were calibrated by the DSO substrate.

atomically resolved *in situ* multifield TEM that can change temperature in conjunction with mechanical conditions. The thermal transition and recovery can be observed at 653 and 593 K, while a more stable vortex is demonstrated at 94 K by cryo-TEM. In the heating process, the out-of-plane lattice of PTO exhibits an anomalous shrinking at high temperature, resulting in a negative thermal coefficient in contrast to the linear increase of STO. At 723 K, the vortices can be restabilized at the nanometer scale by loading in-plane mechanical stress, which would otherwise be degraded. Our finding unravels the competition between Landau and elastic energies in stabilizing the vortex configuration, and brings to the fore the potential vortex-based devices in harsh environments.

ACKNOWLEDGMENTS

This work was supported by the National Key R&D Program of China (Grant No. 2021YFA1400204), the program from the National Natural Science Foundation of China (Grants No. 12334001, No. 51991344, No. 11875229, No. 51872251, and No. 12402190), Chinese Academy of Science (Grants No. XDB33030200 and No. ZDYZ2015-1), the Key R&D Program of Guangdong Province (Grants No. 2018B030327001, No. 2018B010109009, and No. 2019B010931001), Bureau of Industry and Information Technology of Shenzhen (Grant No. 201901161512), Beijing Excellent Talents Training Support (Grant No. 2017000026833ZK11), the Key Research Project of Zhejiang Laboratory (Grant No. 2021PE0AC02), China Postdoctoral Science Foundation (Grants No. 2021M693368 and No. 2022T150692), the RGC Postdoctoral Fellowship Scheme (Grant No. PDFS2223-5S08), the PolyU grant (Grant No. 1-CD4K), and the PolyU Distinguished Postdoctoral Fellowship Scheme (Grant No. 1-YWBC).

X.D.B. and P.G. directed the project. P.C. conceived the idea, analyzed the data, and wrote the paper. P.C. performed the *in situ* experiments with the help of L.L. Z.X. provided support for *in situ* TEM holders. C.T. grew the samples. X.H. and Z.J. carried out the phase-field simulation supervised by J.W., P.C., X.T., J.Z., Y.L., P.G., and X.B. finalized the manuscript. All the authors discussed the results and commented on the manuscript.

The authors declare that they have no competing interests.

[1] A. K. Yadav, C. T. Nelson, S. L. Hsu, Z. Hong, J. D. Clarkson, C. M. Schleputz, A. R. Damodaran, P. Shafer, E. Arenholz, L. R. Dedon, D. Chen, A. Vishwanath, A. M. Minor, L. Q. Chen, J. F. Scott, L. W. Martin, and R. Ramesh, Observation of polar vortices in oxide superlattices, Nature (London) **530**, 198 (2016).

[2] R. Ramesh and D. G. Schlom, Creating emergent phenomena in oxide superlattices, Nat. Rev. Mater. **4**, 257 (2019).

[3] A. K. Yadav, K. X. Nguyen, Z. Hong, P. Garcia-Fernandez, P. Aguado-Puente, C. T. Nelson, S. Das, B. Prasad, D. Kwon, S. Cheema, A. I. Khan, C. Hu, J. Iniguez, J. Junquera, L. Q. Chen, D. A. Muller, R. Ramesh, and S. Salahuddin, Spatially resolved steady-state negative capacitance, Nature (London) **565**, 468 (2019).

[4] S. Das, Z. Hong, V. A. Stoica, M. A. P. Gonçalves, Y. T. Shao, E. Parsonnet, E. J. Marksz, S. Saremi, M. R. McCarter, A. Reynoso, C. J. Long, A. M. Hagerstrom, D. Meyers, V. Ravi, B. Prasad, H. Zhou, Z. Zhang, H. Wen, F. Gómez-Ortiz, P. García-Fernández *et al.*, Local negative permittivity and topological phase transition in polar skyrmions, Nat. Mater. **20**, 194 (2020).

[5] P. Shafer, P. Garcia-Fernandez, P. Aguado-Puente, A. R. Damodaran, A. K. Yadav, C. T. Nelson, S. L. Hsu, J. C. Wojdel, J. Iniguez, L. W. Martin, E. Arenholz, J. Junquera, and R. Ramesh, Emergent chirality in the electric polarization texture of titanate superlattices, Proc. Natl. Acad. Sci. USA **115**, 915 (2018).

[6] L. Van Lich, T. Shimada, J. Wang, V.-H. Dinh, T. Q. Bui, and T. Kitamura, Switching the chirality of a ferroelectric vortex in designed nanostructures by a homogeneous electric field, Phys. Rev. B **96**, 134119 (2017).

[7] P. Behera, M. A. May, F. Gómez-Ortiz, S. Susarla, S. Das, C. T. Nelson, L. Caretta, S.-L. Hsu, M. R. McCarter, B. H. Savitzky, E. S. Barnard, A. Raja, Z. Hong, P. García-Fernandez, S. W. Lovesey, G. van der Laan, P. Ercius, C. Ophus, L. W. Martin, J. Junquera *et al.*, Electric field control of chirality, Sci. Adv. **8**, eabj8030 (2022).

[8] I. I. Naumov, L. Bellaiche, and H. X. Fu, Unusual phase transitions in ferroelectric nanodisks and nanorods, Nature (London) **432**, 737 (2004).

[9] J. Junquera, Y. Nahas, S. Prokhorenko, L. Bellaiche, J. Íñiguez, D. G. Schlom, L.-Q. Chen, S. Salahuddin, D. A. Muller, L. W. Martin, and R. Ramesh, Topological phases in polar oxide nanostructures, Rev. Mod. Phys. **95**, 025001 (2023).

[10] Z. Hong, A. R. Damodaran, F. Xue, S.-L. Hsu, J. Britson, A. K. Yadav, C. T. Nelson, J.-J. Wang, J. F. Scott, L. W. Martin, R. Ramesh, and L.-Q. Chen, Stability of polar vortex lattice in ferroelectric superlattices, Nano Lett. **17**, 2246 (2017).

[11] D. Karpov, Z. Liu, T. d. S. Rolo, R. Harder, P. V. Balachandran, D. Xue, T. Lookman, and E. Fohtung, Three-dimensional imaging of vortex structure in a ferroelectric nanoparticle driven by an electric field, Nat. Commun. **8**, 280 (2017).

[12] P. Chen, X. Zhong, J. A. Zorn, M. Li, Y. Sun, A. Y. Abid, C. Ren, Y. Li, X. Li, X. Ma, J. Wang, K. Liu, Z. Xu, C. Tan, L. Chen, P. Gao, and X. Bai, Atomic imaging of mechanically induced topological transition of ferroelectric vortices, Nat. Commun. **11**, 1840 (2020).

[13] A. R. Damodaran, J. D. Clarkson, Z. Hong, H. Liu, A. K. Yadav, C. T. Nelson, S. L. Hsu, M. R. McCarter, K. D. Park, V. Kravtsov, A. Farhan, Y. Dong, Z. Cai, H. Zhou, P. Aguado-Puente, P. Garcia-Fernandez, J. Iniguez, J. Junquera, A. Scholl, M. B. Raschke *et al.*, Phase coexistence and electric-field control of toroidal order in oxide superlattices, Nat. Mater. **16**, 1003 (2017).

[14] K. Du, M. Zhang, C. Dai, Z. N. Zhou, Y. W. Xie, Z. H. Ren, H. Tian, L. Q. Chen, G. Van Tendeloo, and Z. Zhang, Manipulating topological transformations of polar structures through real-time observation of the dynamic polarization evolution, Nat. Commun. **10**, 4864 (2019).

[15] Z. Hong, S. Das, C. Nelson, A. Yadav, Y. Wu, J. Junquera, L.-Q. Chen, L. W. Martin, and R. Ramesh, Vortex domain walls in ferroelectrics, Nano. Lett. **21**, 3533 (2021).

[16] V. A. Stoica, N. Laanait, C. Dai, Z. Hong, Y. Yuan, Z. Zhang, S. Lei, M. R. McCarter, A. Yadav, A. R. Damodaran, S. Das, G. A. Stone, J. Karapetrova, D. A. Walko, X. Zhang, L. W. Martin, R. Ramesh, L. Q. Chen, H. Wen, V. Gopalan, and J. W. Freeland, Optical creation of a supercrystal with three-dimensional nanoscale periodicity, Nat. Mater. **18**, 377 (2019).

[17] Q. Li, V. A. Stoica, M. Paściak, Y. Zhu, Y. Yuan, T. Yang, M. R. McCarter, S. Das, A. K. Yadav, S. Park, C. Dai, H. J. Lee, Y. Ahn, S. D. Marks, S. Yu, C. Kadlec, T. Sato, M. C. Hoffmann, M. Chollet, M. E. Kozina *et al.*, Subterahertz collective dynamics of polar vortices, Nature (London) **592**, 376 (2021).

[18] Z. Hong and L.-Q. Chen, Blowing polar skyrmion bubbles in oxide superlattices, Acta Mater. **152**, 155 (2018).

[19] L. L. Ma, Y. Ji, W. J. Chen, J. Y. Liu, Y. L. Liu, B. Wang, and Y. Zheng, Direct electrical switching of ferroelectric vortices by a sweeping biased tip, Acta Mater. **158**, 23 (2018).

[20] C. T. Nelson, Z. Hong, C. Zhang, A. K. Yadav, S. Das, S.-L. Hsu, M. Chi, P. D. Rack, L.-Q. Chen, L. W. Martin, and R. Ramesh, In situ electric field manipulation of ferroelectric vortices, Microsc. Microanal. **25**, 1844 (2019).

[21] See Supplemental Material at http://link.aps.org/supplemental/10.1103/PhysRevB.110.195417 for the growth of the sample, details of the in situ TEM, the modeling of phase-field simulations, and supplemental Figs. 1–10, which includes Refs. [22–26].

[22] L.-Q. Chen, APPENDIX A–Landau free-energy coefficients, Phys. Ferroelectrics **105**, 363 (2007).

[23] Y. L. Li, S. Y. Hu, Z. K. Liu, and L. Q. Chen, Effect of substrate constraint on the stability and evolution of ferroelectric domain structures in thin films, Acta Mater. **50**, 395 (2002).

[24] J. Wang, S.-Q. Shi, L.-Q. Chen, Y. Li, and T.-Y. Zhang, Phase-field simulations of ferroelectric/ferroelastic polarization switching, Acta Mater. **52**, 749 (2004).

[25] J. Wang, W. Shu, T. Shimada, T. Kitamura, and T. Y. Zhang, Role of grain orientation distribution in the ferroelectric and ferroelastic domain switching of ferroelectric polycrystals, Acta Mater. **61**, 6037 (2013).

[26] Y. Li, K. Chu, C. Liu, P. Jiang, K. Qu, P. Gao, J. Wang, F. Ren, Q. Sun, L. Chen, and J. Li, Superelastic oxide micropillars enabled by surface tension–modulated 90° domain switching with excellent fatigue resistance, Proc. Natl. Acad. Sci. USA **118**, e2025255118 (2021).

[27] K. J. Choi, M. Biegalski, Y. Li, A. Sharan, J. Schubert, R. Uecker, P. Reiche, Y. Chen, X. Pan, and V. J. S. Gopalan, Enhancement of ferroelectricity in strained $BaTiO_3$ thin films, Science **306**, 1005 (2004).

[28] C. Ederer and N. A. Spaldin, Effect of epitaxial strain on the spontaneous polarization of thin film ferroelectrics, Phys. Rev. Lett. **95**, 257601 (2005).

[29] C. Tan, Y. Dong, Y. Sun, C. Liu, P. Chen, X. Zhong, R. Zhu, M. Liu, J. Zhang, J. Wang, K. Liu, X. Bai, D. Yu, X. Ouyang, J. Wang, P. Gao, Z. Luo, and J. Li, Engineering polar vortex

from topologically trivial domain architecture, Nat. Commun. **12**, 4620 (2021).

[30] Y. L. Tang, Y. L. Zhu, X. L. Ma, and A. Y. Borisevich, Observation of a periodic array of flux-closure quadrants in strained ferroelectric $PbTiO_3$ films, Science **348**, 547 (2015).

[31] C. L. Jia, K. W. Urban, M. Alexe, D. Hesse, and I. Vrejoiu, Direct observation of continuous electric dipole rotation in flux-closure domains in ferroelectric Pb(Zr,Ti) O_3, Science **331**, 1420 (2011).

[32] C. Huang, Z. Liao, M. Li, C. Guan, F. Jin, M. Ye, X. Zeng, T. Zhang, Z. Chen, Y. Qi, P. Gao, and L. Chen, A highly strained phase in $PbZr_{0.2}Ti_{0.8}O_3$ films with enhanced ferroelectric properties, Adv. Sci. **8**, 2003582 (2021).

[33] E. T. Ritz and N. A. Benedek, Strain game revisited for complex oxide thin films: Substrate-film thermal expansion mismatch in $PbTiO_3$, Phys. Rev. Mater. **4**, 084410 (2020).

[34] F.-H. Gong, Y.-L. Tang, Y.-L. Zhu, H. Zhang, Y.-J. Wang, Y.-T. Chen, Y.-P. Feng, M.-J. Zou, B. Wu, W.-R. Geng, Y. Cao, and X.-L. Ma, Atomic mapping of periodic dipole waves in ferroelectric oxide, Sci. Adv. **7**, eabg5503 (2021).

[35] C. Lichtensteiger, J.-M. Triscone, J. Junquera, and P. Ghosez, Ferroelectricity and tetragonality in ultrathin $PbTiO_3$ films, Phys. Rev. Lett. **94**, 047603 (2005).